

Dirac fermions in a Fe ultrathin filmXiao-Tian Zhang,^{1,2} Baolong Xu,^{1,2} Kohji Nakamura,³ and Ryuichi Shindou^{1,2,*}¹*International Center for Quantum Materials, Peking University, Beijing, China*²*Collaborative Innovation Center of Quantum Matter, Beijing, China*³*Department of Physics Engineering, Mie University, Tsu, Mie 514-8507, Japan*

(Received 13 April 2015; revised manuscript received 31 August 2015; published 16 September 2015)

We show the existence of massive Dirac fermions in the electronic band structures of a few Fe atomic layers with perpendicular magnetization. Based on a tight-binding model fitted to *ab initio* band structure, we observe four distinct massive Dirac fermions near the Fermi level, which result from atomic spin-orbit coupling of Fe and a band inversion between an Fe $4s$ - $3d_{x^2-y^2}$ hybrid orbital band and a $3d_{xy}$ orbital band. These led to a valence band with a finite Chern integer (+2) and chiral edge modes near the Fermi level. When the chemical potential is set inside the Dirac gap by carrier doping, the Hall conductivity exhibits a plateaulike structure with a quantized value $2(e^2/h)$, and orbital magnetization shows a prominent increase, the latter of which is mostly due to the chiral orbital motion of electrons along the edge modes. We discuss the stability of the Dirac fermions in the Fe(001) monolayer on an MgO(001) substrate and an Fe(001) bilayer case.

DOI: [10.1103/PhysRevB.92.094429](https://doi.org/10.1103/PhysRevB.92.094429)

PACS number(s): 73.61.-r, 75.70.Ak, 75.70.Rf, 75.70.Tj

I. INTRODUCTION

Since the discovery of graphene [1,2], a number of novel two-dimensional electronic phases have been theoretically proposed [3,4]. Such efforts include a proposal of a so-called ‘‘Chern insulator’’ in graphene with ferromagnetic substrates. Thereby, it was theoretically proposed that the magnetic proximity effect from the substrate in combination with atomic spin-orbit interaction of a carbon atom could give rise to a finite mass gap in the Dirac fermion of graphene, resulting in quantized Hall conductance [5,6]. From experimental point of view, a few atomic layers of $3d$ -electron ferromagnets themselves, such as Fe, Co, and Ni and their alloys, can be easily grown on various substrates [7]. When the thickness of the magnetic layers reaches atomic scale, magnetic anisotropy energy associated with surface magnetism dominates over magnetostatic energy, often causing the magnetic easy axis to be perpendicular to the layer [perpendicular magnetic anisotropy (PMA)] [8–27]. To obtain a comprehensive understanding of the PMA phenomenon, it is also important to extract common features in the electronic band structures of a few atomic layers of d -electron ferromagnets, such as Fe, Co, and Ni.

In this paper, we show the existence of massive Dirac fermions near the Fermi level in the electronic band structures of bcc Fe(001) of a few atomic layers with perpendicular magnetization (Fig. 1). The Dirac fermions are well described by a three-orbital tight-binding model composed of $3d_{xy}$, $3d_{x^2-y^2}$, and $4s$ orbitals of an Fe atom, where an atomic spin-orbit interaction of Fe and a band inversion between a $3d_{xy}$ orbital band and a $4s$ - $3d_{x^2-y^2}$ hybrid-orbital band play an essential role for the emergence of the Dirac fermions. From *ab initio* band calculations, the mass of the Dirac fermions is estimated to be around 80 meV (60 meV) for a Fe monolayer without (with) an MgO(001) substrate. In a free-standing

Fe(001) monolayer, the massive Dirac fermion results in a plateaulike feature in Hall conductivity and $dM_{\text{orb}}/d\mu$ near the Fermi level, where M_{orb} denotes the out-of-plane orbital magnetization and μ denotes the the chemical potential. In experiments, the chemical potential can be controlled by an electric gate voltage (out-of-plane electric field). It is shown that the Dirac fermions in Fe monolayers are robust against broken out-of-plane inversion symmetry induced by the electric voltage. A comparison with existing *ab initio* band calculations [16,28] suggests that the Dirac fermions of the same origin can also be found in the electronic band structures of bcc Co(001) and hcp Co(111) monolayers.

II. ELECTRONIC BAND STRUCTURE

Ab initio calculations are performed using film full-potential linearized augmented plane wave (FLAPW) method [29–31] based on the local-spin-density approximation (LSDA) [32], in which the core states are treated fully relativistically and the valence states are treated semirelativistically. LAPW functions with a cutoff of $|\mathbf{k} + \mathbf{G}| \leq 3.9$ a.u.⁻¹ and muffin-tin sphere radii of 2.2, 2.2, and 1.4 a.u. for Fe, Mg, and O atoms are used, where the angular momentum expansion inside the MT spheres is truncated at $\ell = 8$ (Fe and Mg) and $\ell = 6$ (O) for the wave functions, charge density, and potential. The Fe/MgO was modeled by an Fe monolayer on a six-atomic-layer MgO(001) substrate, where Fe atoms are located on top of the O atoms, assuming the in-plane lattice constant matching to the calculated value of bulk MgO while the out-of-plane coordinates of Fe atoms are fully optimized using the atomic-force FLAPW calculations. Note that the structural parameters obtained within the LSDA agree qualitatively with those analyzed by surface x-ray diffraction [33] as demonstrated previously [53].

The *ab initio* electronic band structure for minority-spin bands of a free-standing Fe monolayer with perpendicular magnetization is fitted near the Fermi level with a tight-binding model composed of five $3d$ orbitals, $4s$, $4p_x$, and $4p_y$ orbitals

*Author to whom all correspondence should be addressed: rshindou@pku.edu.cn

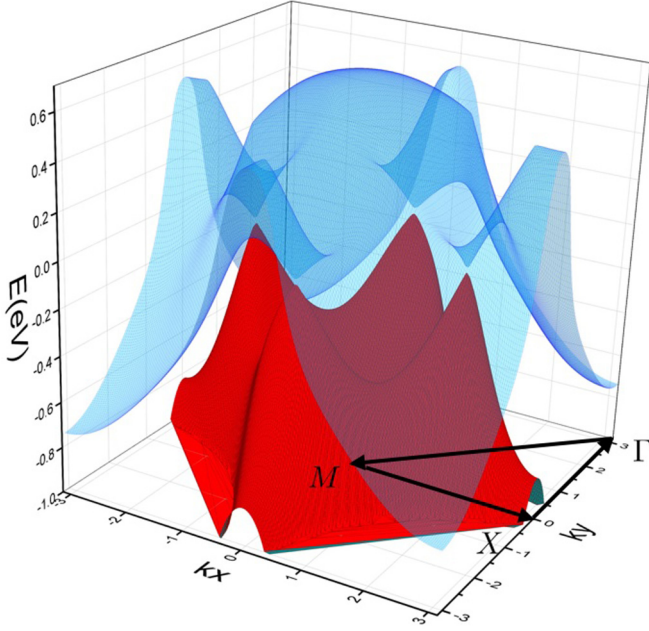


FIG. 1. (Color online) Four massive Dirac fermions in the electronic band structure of a perpendicularly magnetized free-standing Fe monolayer.

of an Fe atom,

$$\hat{H} = \sum_{i,m} \epsilon_{m\uparrow} \hat{c}_{i,m\uparrow}^\dagger \hat{c}_{i,m\uparrow} + \sum_{\langle\langle i,j \rangle\rangle; mn} t_{ij;mn\uparrow} \hat{c}_{i,m\uparrow}^\dagger \hat{c}_{j,n\uparrow} + \lambda_{so} \sum_{i;mn} \hat{c}_{i,m\uparrow}^\dagger [\mathbf{L}]_{mn} \cdot [\mathbf{S}]_{\uparrow} \hat{c}_{i,n\uparrow}. \quad (1)$$

$\hat{c}_{i,m\uparrow}^\dagger$ ($\hat{c}_{i,m\uparrow}$) is the electron creation (annihilation) operator on site i , for orbital m , and spin up (where the spin-quantization axis is taken along the perpendicular magnetization direction, the z direction). The first term represents an effective atomic energy of each orbital, which includes all the on-site-type energies felt by the respective orbital, such as exchange splitting energy from majority-spin electrons and crystal fields caused by surrounding electrons. The second term represents the neighboring hopping term with interatomic (intra-atomic) transfer integrals $t_{ij;mn\uparrow}$. The angular brackets in $\langle\langle i,j \rangle\rangle$ stand for summation of nearest-neighboring and next-nearest-neighboring sites. The third term is the atomic spin-orbit coupling with coupling strength taken to be $\lambda_{so} = 50$ meV. Since an exchange splitting between majority-spin bands and minority-spin bands estimated from *ab initio* band calculations is about 3 eV, being 60 times larger than the atomic spin-orbit coupling strength of Fe, we consider only the diagonal part of spin-orbit interactions with respect to the spin index; an expected correction due to the off-diagonal parts, $[\mathbf{L}_\pm][\mathbf{S}_\mp]$, is evaluated to be on the order of 1 meV, being fairly negligible compared to that from the diagonal part. The interatomic transfer integrals $t_{ij;mn\uparrow}$ are given by matrix elements in the Slater-Koster table [34], such as V_{sd} , V_{sp} , $V_{dd\sigma}$, $V_{dd\pi}$, $V_{dd\delta}$, and so on. These matrix elements in the Slater-Koster table along with the effective atomic energies $\epsilon_{m\uparrow}$ are used as fitting parameters, whose best-fit values in the absence of spin-orbit interaction are shown in Table I. The table shows reasonable

TABLE I. Upper: Tight-binding hopping parameters for minority spin bands, obtained from the fitting to the LSDA calculation. The energy unit is eV. Lower: On-site effective atomic energies for minority-spin $3d$ electrons and $4s$, $4p_x$, and $4p_y$ electrons.

	σ	π	δ				
Fe d -Fe d (NN)	-0.363	0.261	-0.061				
Fe d -Fe d (NNN)	-0.080	0.064	-0.025				
Fe p -Fe d (NN)	-0.392	0.157					
Fe p -Fe d (NNN)	-0.118	0.047					
Fe p -Fe p (NN)	2.905	-1.063					
Fe s -Fe d (NN)	-0.392						
Fe s -Fe d (NNN)	-0.118						
Fe s -Fe s (NN)	-1.419						
Fe s -Fe p (NN)	2.208						
	s	p	d_{z^2}	d_{xz}	d_{yz}	$d_{x^2-y^2}$	d_{xy}
$\epsilon_{i,\uparrow}$	2.315	8.915	0.350	0.233	0.234	0.160	0.463

fitting values compared to the solid state table [34] and the lattice constant of the square-lattice Fe monolayer evaluated from the same first-principles calculation ($a = 2.95$ Å).

Figure 2(a) plots the band structure along high-symmetry k points obtained from both our eight-band tight-binding model and LSDA calculations with $\lambda_{so} = 0$. Notably, there exist four linearly dispersive band crossings along the zone boundary connecting the M point and the X point near the Fermi level. As shown below, these linear dispersions are well described by massless Dirac fermions without the spin-orbit interaction. With the atomic spin-orbit interaction, each massless Dirac fermion acquires the same sign of the mass, endowing a valence band with a finite Chern number +2.

The four Dirac cones are enveloped by two other dispersive bands composed of d_{xz} and d_{yz} , while the out-of-plane mirror symmetry allows us to treat these two bands separately from the other six bands composed of s , $d_{x^2-y^2}$, d_{xy} , p_x , p_y , and d_{z^2} , because $\langle z \text{ odd} | \hat{H} | z \text{ even} \rangle = \langle z \text{ odd} | \hat{\sigma}_z \hat{\sigma}_z \hat{H} \hat{\sigma}_z \hat{\sigma}_z | z \text{ even} \rangle = -\langle z \text{ odd} | \hat{H} | z \text{ even} \rangle = 0$. The presence of a substrate, such as MgO(001), breaks the out-of-plane mirror symmetry, giving rise to a finite mixing between these two groups of bands, while, more importantly, the oxide substrate endows with relatively strong charging energies the out-of-plane d orbitals, such as d_{xz} , d_{yz} , and d_{z^2} . Thus, d_{xz} - d_{yz} bands are brought into a higher-energy region, while the four Dirac fermions composed by $4s$, $3d_{x^2-y^2}$, and $3d_{xy}$ remain intact [Fig. 2(c)]. For the sake of clarity, we consider in the following a free-standing Fe monolayer and treat these two groups of bands separately, unless dictated otherwise. The case with the MgO(001) substrate will be discussed later more carefully.

III. BAND INVERSION MECHANISM

The emergence of the Dirac fermions and the valence band acquiring the Chern number +2 result from (i) a band inversion between a $3d_{xy}$ orbital band and a $4s$ - $3d_{x^2-y^2}$ hybrid-orbital band, and (ii) a complex-valued band mixing between these

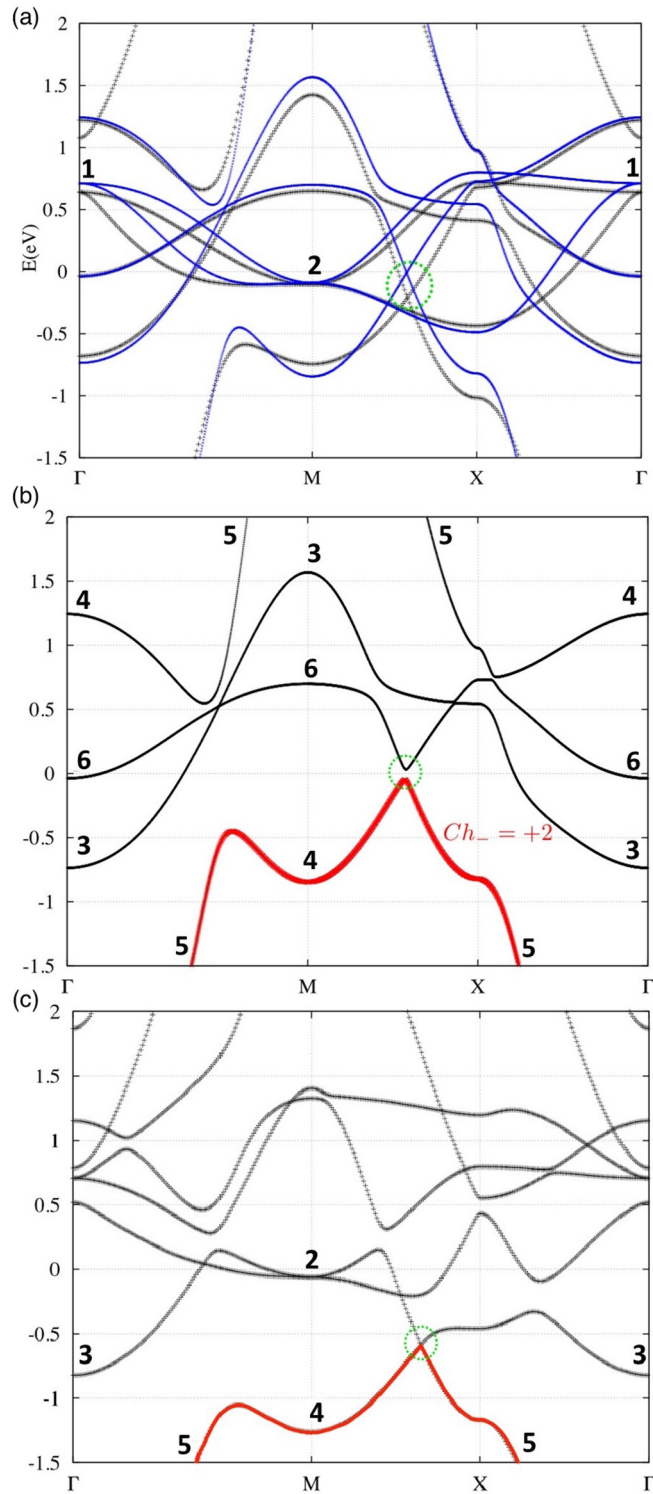


FIG. 2. (Color online) (a) Electronic band structures for minority spin near the Fermi level (without atomic SOI) from LSDA calculation (black) and the eight-band tight-binding model (blue). The Dirac fermion is depicted by a green circle. (b) From the six-band tight-binding model (with atomic SOI). The lowest band, which acquires the Chern number 2, is drawn with a red bold line. The massive Dirac fermions are depicted by a green circle. (c) From LSDA calculation with MgO(001) substrate and without atomic SOI. The orbital characters of bands labeled as 1 and 2 are $3d_{xz}$ and $3d_{yz}$, while those of 3, 4, 5, and 6 are $3d_{x^2-y^2}$, $3d_{xy}$, $4s$, and $3d_{z^2}$, respectively.

two bands mediated by the atomic spin orbital interaction. Due to the orbital symmetry, the nearest-neighbor intraorbital transfer integrals make the hybrid orbital band to have positive curvature at the Γ point and negative curvature at the M point, while the $3d_{xy}$ orbital band has negative curvature at the Γ point and positive curvature at the M point. As a result, the hybrid-orbital band is lower in energy than the $3d_{xy}$ orbital band at the Γ point, while it is higher than $3d_{xy}$ at the M point (“band inversion”).

In the presence of the atomic spin-orbit interaction with the out-of-plane ferromagnetic moment, the d_{xy} orbital is mixed with the $d_{x^2-y^2}$ orbital character with a pure imaginary coefficient, i.e., $d_{xy} \rightarrow d_{xy} + i\alpha d_{x^2-y^2}$, with α proportional to the spin-orbit interaction. Because of this mixing, the hybrid orbital band and the $3d_{xy}$ orbital band acquire a complex-valued band mixing, which takes the form of $t' \sin k_x \sin k_y + iat(\cos k_x - \cos k_y)$ in momentum space; $\sin k_x \sin k_y$ and $\cos k_x - \cos k_y$ are from the $3d_{xy}$ and $3d_{x^2-y^2}$ orbital symmetry, respectively. As shown below, the band inversion and the complex-valued band mixing result in the valence band with Chern number +2.

The valence band with Chern number +2 can be well described by the lowest energy band of a three-band tight-binding model composed of $4s$, $3d_{xy}$, and $3d_{x^2-y^2}$ orbitals. In the momentum space, the model takes the form

$$H^{3 \times 3}(\mathbf{k}) = \begin{pmatrix} E_s(\mathbf{k}) & -2\sqrt{3}V'_{sd}s_x s_y & \sqrt{3}V_{sd}(c_x - c_y) \\ * & E_{xy}(\mathbf{k}) & -2i\lambda_{so} \\ * & * & E_{x^2-y^2}(\mathbf{k}) \end{pmatrix}, \quad (2)$$

where $E_i(\mathbf{k}) = \mathcal{E}_i + t_i(c_x + c_y) + 2t'_i c_x c_y$, $c_{x,y} \equiv \cos k_{x,y}$, $s_{x,y} \equiv \sin k_{x,y}$, with subindex $i = s, xy$, and $x^2 - y^2$ representing $4s$, $3d_{xy}$, and $3d_{x^2-y^2}$ orbitals. \mathcal{E}_i denotes their effective atomic energies, and t_i and t'_i denote their nearest- and next-nearest-neighbor intraorbital transfer integrals. The lowest band energy of Eq. (2) will be denoted as $E_-(\mathbf{k})$ henceforth.

To see the band topology for the lowest band, let us first derive an effective 2×2 Hamiltonian out of $H^{3 \times 3}(\mathbf{k})$. Toward that end, notice first that the lowest band energy is always smaller than $E_s(\mathbf{k})$, $E_{xy}(\mathbf{k})$, and $E_{x^2-y^2}(\mathbf{k})$ for all \mathbf{k} ; $E_- < \min(E_s, E_{xy}, E_{x^2-y^2})$. On such an occasion, we may describe the lowest band by treating either one of these three orbitals as a high-energy degree and deriving an effective 2×2 Hamiltonian for the other two; the lowest band of $H^{3 \times 3}(\mathbf{k})$ is identified with that of the 2×2 Hamiltonian. As shown in Figs. 2(b) and 3, the focused valence band has mainly $4s$ and $3d_{xy}$ characters. Thus, we regard the $3d_{x^2-y^2}$ orbital as the high-energy degree of freedom and treat its couplings with $4s$ and $3d_{xy}$ as perturbations. This leads to the 2×2 effective Hamiltonian for the “ $4s$ band” and the $3d_{xy}$ band. Quantitatively speaking, the “ $4s$ band” thus introduced is a $4s$ - $3d_{x^2-y^2}$ hybrid-orbital band rather than purely a $4s$ orbital band, because of larger mixing between $4s$ and $3d_{x^2-y^2}$ coming from $V_{sd} (\gg \lambda_{so})$. In fact, the hybrid band has a larger $3d_{x^2-y^2}$ orbital character than the $4s$ orbital in a certain momentum region (see Fig. 3).

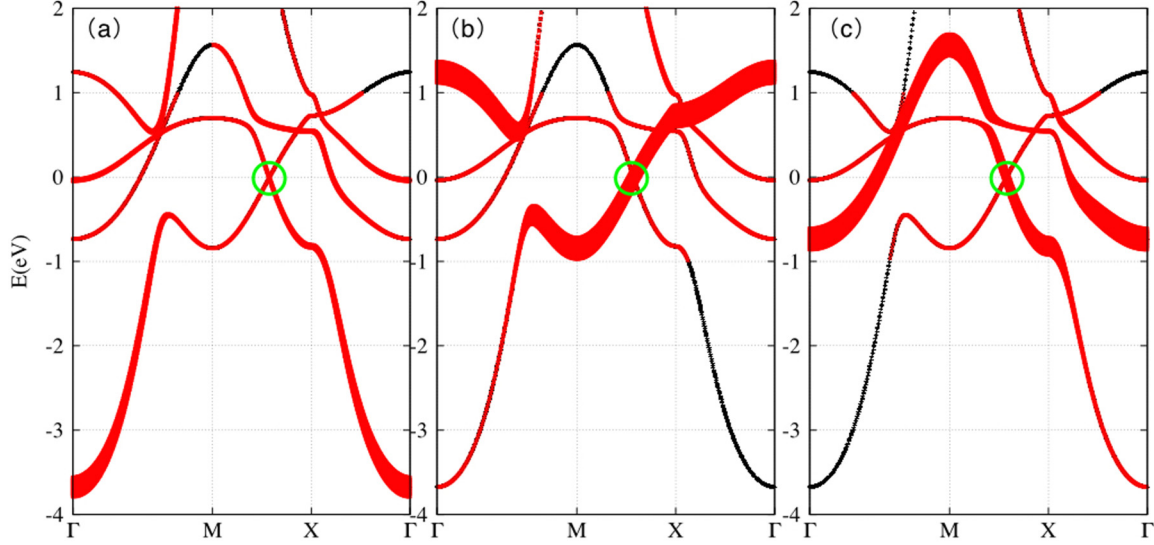


FIG. 3. (Color online) “Fat-band” picture obtained from the six-band tight-binding model. The respective orbital character is depicted by the linewidth (red) in (a) for $4s$, in (b) for $3d_{x^2-y^2}$, and in (c) for $3d_{xy}$.

The degenerate perturbation theory gives the 2×2 Hamiltonian as follows:

$$\langle i | H_{\text{eff}}^{2 \times 2} | j \rangle = \langle i | H_0 | j \rangle + \frac{\langle i | H_1 | x^2 - y^2 \rangle \langle x^2 - y^2 | H_1 | j \rangle}{E - E_{x^2-y^2}(\mathbf{k})} \quad (3)$$

with $i, j = s, xy$ and

$$H_0 \equiv \begin{pmatrix} E_s(\mathbf{k}) & -2\sqrt{3}V'_{sd}s_x s_y & 0 \\ -2\sqrt{3}V'_{sd}s_x s_y & E_{xy}(\mathbf{k}) & 0 \\ 0 & 0 & E_{x^2-y^2}(\mathbf{k}) \end{pmatrix}, \quad (4)$$

$$H_1 \equiv \begin{pmatrix} 0 & 0 & \sqrt{3}V_{sd}(c_x - c_y) \\ 0 & 0 & -2i\lambda_{so} \\ \sqrt{3}V_{sd}(c_x - c_y) & 2i\lambda_{so} & 0 \end{pmatrix}. \quad (5)$$

Equivalently,

$$H_{\text{eff}}^{2 \times 2} = \begin{pmatrix} \bar{E}_s(\mathbf{k}) & \bar{E}_{s,xy}(\mathbf{k}) \\ \bar{E}_{s,xy}^*(\mathbf{k}) & \bar{E}_{xy}(\mathbf{k}) \end{pmatrix}, \quad (6)$$

with

$$\bar{E}_s = E_s - \frac{3V_{sd}^2(c_x - c_y)^2}{\Delta E}, \quad \bar{E}_{xy} = E_{xy} - \frac{4\lambda_{so}^2}{\Delta E},$$

$$\bar{E}_{s,xy} = -2\sqrt{3}V'_{sd}s_x s_y - \frac{i2\sqrt{3}\lambda_{so}V_{sd}(c_x - c_y)}{\Delta E}.$$

The perturbation treatment is valid as far as $\Delta E \equiv E_{x^2-y^2}(\mathbf{k}) - E$ is positive. This condition is satisfied for any \mathbf{k} when $E = E_-(\mathbf{k})$.

The 2×2 Hamiltonian has two eigenvalues whose smaller one corresponds to the lowest band energy of $H^{3 \times 3}(\mathbf{k})$. Thereby, $E_-(\mathbf{k})$ can be obtained from the following

self-consistent equation of E_- :

$$2E_-(\mathbf{k}) = \bar{E}_s(\mathbf{k}) + \bar{E}_{xy}(\mathbf{k}) - \sqrt{[\bar{E}_s(\mathbf{k}) - \bar{E}_{xy}(\mathbf{k})]^2 + 4|\bar{E}_{s,xy}(\mathbf{k})|^2},$$

where the right-hand side is given by $E_-(\mathbf{k})$ itself by way of $\Delta E \equiv E_{x^2-y^2}(\mathbf{k}) - E_-(\mathbf{k})$. The equation has a solution for E_- that always satisfies $E_- < \min(E_s, E_{xy}, E_{x^2-y^2})$ for any \mathbf{k} , justifying *a posteriori* the validity of the perturbative treatment.

With this justification in mind, we can readily identify the band topology of the lowest energy band of $H_{\text{eff}}^{2 \times 2}(\mathbf{k})$ as that of $H^{3 \times 3}(\mathbf{k})$. As is clear from Fig. 2(b), the hybrid band becomes lower in energy than the $3d_{xy}$ band at the Γ point; $\bar{E}_s < \bar{E}_{xy}$ at $\mathbf{k} = \Gamma$, while otherwise at the M point; $\bar{E}_s > \bar{E}_{xy}$ at $\mathbf{k} = M$. Between the Γ and M points, these two bands have a mixing due to a finite off-diagonal matrix element $\bar{E}_{s,xy}(\mathbf{k})$. Importantly, the matrix element has a complex phase, which acquires the 4π phase, whenever \mathbf{k} goes around the Γ point (or the M point),

$$\oint_{\partial S} \nabla_{\mathbf{k}} \{\arg \bar{E}_{s,xy}(\mathbf{k})\} \cdot d\mathbf{k} = 4\pi, \quad (7)$$

where ∂S denotes an arbitrary loop that encompasses the Γ point (or the M point).

The 4π phase winding of the interband matrix element and the band inversion between the hybrid band and the $3d_{xy}$ band endow the lowest band with the Chern number $+2$. To see this, expand the 2×2 Hamiltonian in terms of the Pauli matrix, $H_{\text{eff}}^{2 \times 2}(\mathbf{k}) = a_0(\mathbf{k})\sigma_0 + \mathbf{a}(\mathbf{k}) \cdot \boldsymbol{\sigma}$, from which the normalized vector $\mathbf{n}(\mathbf{k})$ is introduced by $\mathbf{n} \equiv \mathbf{a}/|\mathbf{a}|$. According to the projective representation of the Chern invariants [35–37], the Chern number for the lowest band (Ch_-) is given by an integral of a solid angle subtended by the unit vector over the first Brillouin zone; $\text{Ch}_- \equiv \frac{1}{4\pi} \int_{\text{BZ}} dk_x dk_y \mathbf{n}(\mathbf{k}) \cdot [\partial_{k_x} \mathbf{n}(\mathbf{k}) \times \partial_{k_y} \mathbf{n}(\mathbf{k})]$. The integral is quantized to be an integer, which counts how many times the unit vector wraps the unit sphere when the momentum \mathbf{k} wraps the first Brillouin zone once. Now that

$\bar{E}_s < \bar{E}_{xy}$ and $\bar{E}_{s,xy} = 0$ at the Γ point while $\bar{E}_s > \bar{E}_{xy}$ and $\bar{E}_{s,xy} = 0$ at the M point, the unit vector points to the south pole (north pole) of the unit sphere when \mathbf{k} at the Γ (M) point, respectively. On the one hand, Eq. (7) means that the unit vector always winds *twice* around the pole when \mathbf{k} rotates once around the Γ point. This dictates that the Chern integer for the lowest band is $+2$.

The lowest band forms four distinct Dirac fermions along the Brillouin zone boundary, $\{\mathbf{K}_1, \mathbf{K}_2, \mathbf{K}_3, \mathbf{K}_4\} = \{(\pi, K), (\pi, -K), (K, \pi), (-K, \pi)\}$. Around each Dirac point, the effective 3×3 Hamiltonian conceiving the Dirac fermion is linearly expanded in small q_x, q_y , and λ_{so} , e.g.,

$$H_{\text{eff}}^{3 \times 3}(\mathbf{k}) = M_1(q_x a)\sigma_x + M_2\lambda_{so}\sigma_y + M_3(q_y a)\sigma_z + \dots \quad (8)$$

with $\mathbf{k} \equiv \mathbf{q} + \mathbf{K}_1$, and $M_1 = -0.34$ eV, $M_2 = -0.97$, and $M_3 = -0.66$ eV for the tight-binding parameters in Table I.

The four Dirac points play the role of dual magnetic monopoles in a three-dimensional parameter space subtended by k_x, k_y , and λ_{so} [38–41]. The corresponding magnetic field $\mathbf{B}_-(\mathbf{k}, \lambda_{so})$ is associated with a Bloch wave function for the lowest band, $|u_-(\mathbf{k}, \lambda_{so})\rangle$ with $H(\mathbf{k}, \lambda_{so})|u_-\rangle = E_-|u_-\rangle$. The magnetic field is a rotation of a three-component gauge field $\mathbf{A}_-(\mathbf{k}, \lambda_{so})$, $\mathbf{B}_-(\mathbf{k}, \lambda_{so}) = \nabla \times \mathbf{A}_-(\mathbf{k}, \lambda_{so})$ with $\nabla \equiv (\partial_{k_x}, \partial_{k_y}, \partial_{\lambda_{so}})$. $\mathbf{A}_-(\mathbf{k}, \lambda_{so})$ are gauge connections of the Bloch wave function: $\mathbf{A}_- = i\langle u_- | \nabla | u_- \rangle$. Due to the fourfold rotational symmetry, dual magnetic charges at four Dirac points have the same quantized strength 2π , where their sign is the same as $-\text{sgn}[M_1 M_2 M_3]$ (Fig. 4),

$$\nabla \cdot \mathbf{B}_-(\mathbf{k}, \lambda_{so}) = 2\pi \sum_{j=1}^4 \delta(\lambda_{so})\delta(\mathbf{k} - \mathbf{K}_j). \quad (9)$$

The Chern integer for the lowest band is the total magnetic flux penetrating through the constant λ_{so} plane in 3D space,

$$\text{Ch}_-(\lambda_{so}) = \int_{\text{BZ}} \frac{d\mathbf{k}}{2\pi} (\partial_{k_x} A_{-,y}(\mathbf{k}, \lambda_{so}) - \partial_{k_y} A_{-,x}(\mathbf{k}, \lambda_{so})).$$

When λ_{so} goes across the $\lambda_{so} = 0$ plane, the Chern integer changes by -4 (Fig. 4),

$$\text{Ch}_-(\lambda_{so} < 0) - \text{Ch}_-(\lambda_{so} > 0) = -4. \quad (10)$$

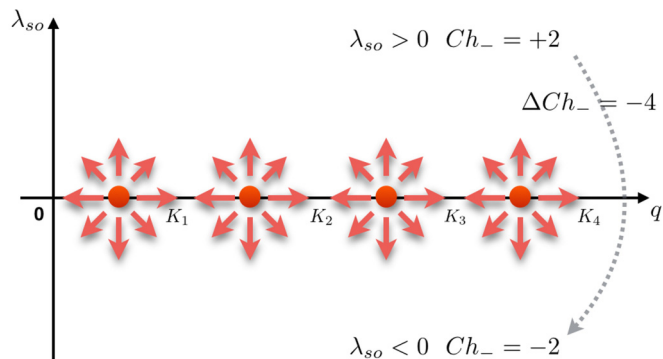


FIG. 4. (Color online) Schematic picture of dual magnetic magnetic charges and dual magnetic field in the three-dimensional space subtended by k_x, k_y , and λ_{so} . The Chern integer for each λ_{so} is given by the surface integral of the field over the first Brillouin zone for the constant λ_{so} .

The time-reversal symmetry connects the spinless tight-binding Hamiltonian for $\lambda_{so} > 0$ and that for $\lambda_{so} < 0$ with the relation $H^*(\mathbf{k}, \lambda_{so}) = H(-\mathbf{k}, -\lambda_{so})$, which leads to $\text{Ch}_-(\lambda_{so}) = -\text{Ch}_-(\lambda_{so})$. Combing this with Eq. (10), we have $\text{Ch}_-(\lambda_{so} > 0) = +2$.

IV. HALL CONDUCTIVITY AND ORBITAL MAGNETIZATION

The hallmark of the existence of massive Dirac fermions is transverse conductivity [38,39,42]. Hall conductivity as a function of the chemical potential is calculated for the eight-band tight-binding model for a free-standing Fe monolayer (Fig. 5) with

$$\sigma_{xy} = \frac{e^2}{h} \sum_n^{\varepsilon_n < \mu} \int_{\text{BZ}} \frac{d\mathbf{k}}{2\pi} (\partial_{k_x} A_{n,y} - \partial_{k_y} A_{n,x}),$$

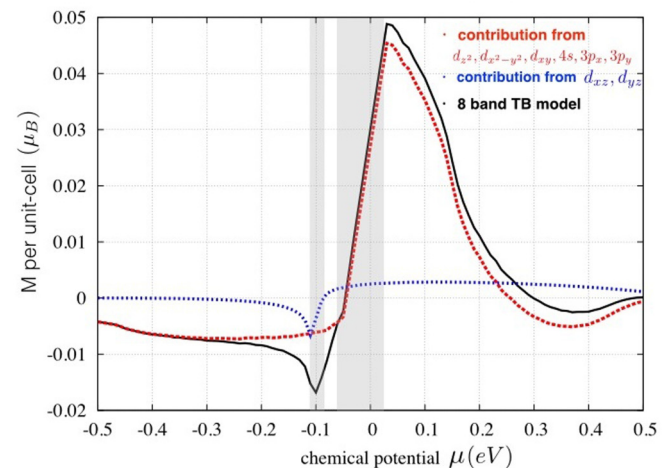
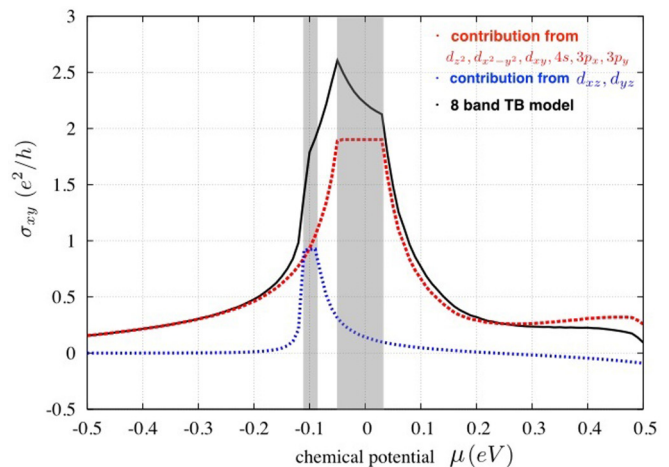


FIG. 5. (Color online) Upper (lower): Hall conductivity (orbital magnetization) as a function of the chemical potential for the eight-band tight-binding model for a free-standing Fe monolayer. Due to the out-of-plane mirror symmetry, the contribution can be decomposed into that from the six-band electronic states ($3d_{xy}, 3d_{x^2-y^2}, 3d_{z^2}, 4s, 4p_x, 4p_y$; red color) and that from the two-band electronic states ($3d_{xz}, 3d_{yz}$; blue color). The direct-band-gap region associated with the massive Dirac fermions is specified by a gray-hatched energy window, $[-0.05 \text{ eV}, 0.03 \text{ eV}]$.

where $A_{n,\mu} \equiv i \langle u_n | \partial_{k_\mu} | u_n \rangle$ with $H(\mathbf{k}) | u_n(\mathbf{k}) \rangle \equiv \mathcal{E}_n | u_n(\mathbf{k}) \rangle$; n is the band index. Due to the out-of-plane mirror symmetry, the conductivity can be decomposed into the two-band contribution (from $3d_{zx}$ and $3d_{yz}$ orbitals) and the six-band contribution (from $4s$, $3d_{x^2-y^2}$, $3d_{xy}$, $3d_{z^2}$, $4p_x$, and $4p_y$ orbitals). When the chemical potential is inside the Dirac gap ($\mu \simeq 0$), the Hall conductivity shows a prominent peak structure with a maximum value around $2e^2/h$. The peak structure is mainly due to a nearly quantized contribution from the six-band electronic states. The quantized value is approximately $2e^2/h$, which is a direct consequence of the four massive Dirac fermions near $\mu = 0$. A slight deviation from the quantization is attributed to another small but nonvanishing dual magnetic field associated with a dispersive band near the Γ point.

The two-band electronic state also gives a nearly quantized contribution e^2/h to the Hall conductivity near the Fermi level ($\mu \simeq -0.1$ eV); $3d_{xz}$ and $3d_{yz}$ orbital bands comprise another SOI-induced direct band gap at the M point. The tight-binding Hamiltonian for $3d_{xz}$ and $3d_{yz}$ orbitals is expanded linearly in small $q_x q_y$, $q_x^2 - q_y^2$, and λ_{so} with $\mathbf{k} = \mathbf{q} + (\pi, \pi)$;

$$H(\mathbf{k}) = \lambda_{so} \sigma_y + (V'_{dd\delta} - V'_{dd\pi})(q_x a)(q_y a) \sigma_x \\ + (V_{dd\pi} - V_{dd\delta}) \frac{(q_x a)^2 - (q_y a)^2}{2} \sigma_z + \dots,$$

where $V'_{dd\pi}$ and $V'_{dd\delta}$ denote the Slater-Koster hopping parameters between the (next)-nearest-neighboring Fe d orbitals. The expansion dictates that the dual magnetic fields for the two bands have 4π magnetic charge at the M point on the $\lambda_{so} = 0$ plane. This, in combination with the symmetry property $H^*(\mathbf{k}, \lambda_{so}) = H(-\mathbf{k}, -\lambda_{so})$, requires that the integral of the dual magnetic field ($\partial_{k_x} A_{n,y} - \partial_{k_y} A_{n,x}$; n is either lower or higher band out of the two bands) near the M point is quantized to be 2π in the smaller λ_{so} limit. When the chemical potential is inside the SOI-induced gap at the M point, one of the two bands is partially filled while the other is empty. Since a Fermi surface associated with the filled band is large enough compared to a distribution of the magnetic flux around the M point, the Hall conductivity from the two-band electronic state is nearly quantized to be e^2/h as in Fig. 5.

The emergence of the massive Dirac fermions also results in peculiar chiral modes localized near the boundary of a two-dimensional Fe monolayer. Figure 6 shows the electronic band structure of the six-band tight-binding model with a periodic (open) boundary condition along the x (y) direction of the square-lattice Fe monolayer. When projected onto a surface crystal momentum axis, the four massive Dirac fermions at $\mathbf{k} = \mathbf{K}_1, \mathbf{K}_2, \mathbf{K}_3, \mathbf{K}_4$ reduce to three distinct valleys with a direct band gap, located at $k_x = \pi, \pm K$, respectively. Now that the gap endows the lower bulk band with the Chern number $+2$ as described above, the bulk-edge correspondence [43–46] dictates that two localized chiral edge modes appear in the direct band gap of the three valleys [Fig. 6(b)]. In the present case, the direct band gap is also masked by another dispersive bulk band located at the Γ point, mainly composed of a $3d_{x^2-y^2}$ orbital (Fig. 2). As a result, the chiral edge modes are terminated by the dispersive bulk band around $k_x = 0$ [Figs. 6(a) and 6(c)].

The chiral modes give rise to large out-of-plane orbital magnetization when the chemical potential μ is set inside the

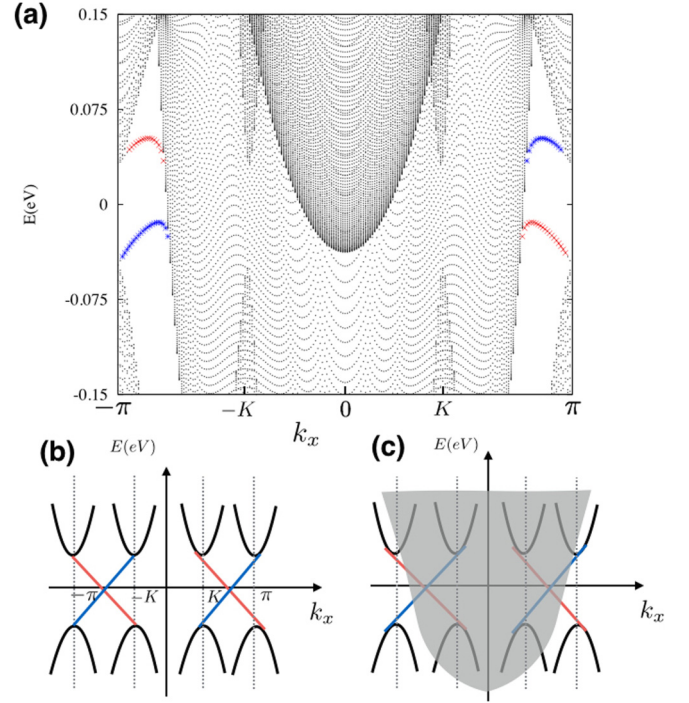


FIG. 6. (Color online) (a) Electronic band structure obtained from the tight-binding model with a finite slab geometry and periodic boundary condition along the x direction. The black colored points are extended over the two-dimensional bulk, while the red (blue) color points are for those eigenstates localized at one (the other) boundary ($y = 0$ or $y = L$) with $L = 200$. Two chiral edge modes are terminated by a bulk band near $k = 0$. (b) Schematic picture of an expected band structure (b) without the bulk band near $k = 0$. (c) With the bulk band near $k = 0$, where two chiral edge modes (partially) go across the direct band gap associated with massive Dirac fermions.

Dirac gap. When increasing μ inside the gap, electrons are added up into the edge modes, which enhances chiral electric currents flowing around the boundary of the two-dimensional system. Irrespective of the details of the energy dispersion of the chiral modes, the increase of the current is proportional to the increase of μ . Such chiral edge current contributes to a macroscopic orbital moment $\langle r \times p \rangle$ [47–50], which results in a linear increase of the magnetic moment with respect to the carrier doping near the Fermi level. To see this situation, we have calculated the orbital magnetization based on the Streda formula [51,52]. The magnetization is the derivative of the free energy in the magnetic field H , while the total number of electrons N is the derivative in μ . This leads to $\partial N / \partial H = \partial M / \partial \mu$, provided that the free energy is analytic in μ and H . According to Streda [51], $\partial N / \partial H$ can be expressed only in terms of the current operators,

$$\frac{\partial M}{\partial \mu} = \frac{1}{ec} \left\{ \sigma_{xy}(\mu) - \frac{i\hbar}{2} \text{Tr}[J_x G^+(\mu) J_y \delta(\mu - \mathcal{H}) - \text{H.c.}] \right\}, \quad (11)$$

where J_v is the current operator ($v = x, y$), and $G^\pm(\mu) \equiv 1/[(\mu \pm i\delta)I - \mathcal{H}]$ and \mathcal{H} are the lesser and greater single-particle Green functions and Hamiltonian, respectively. By

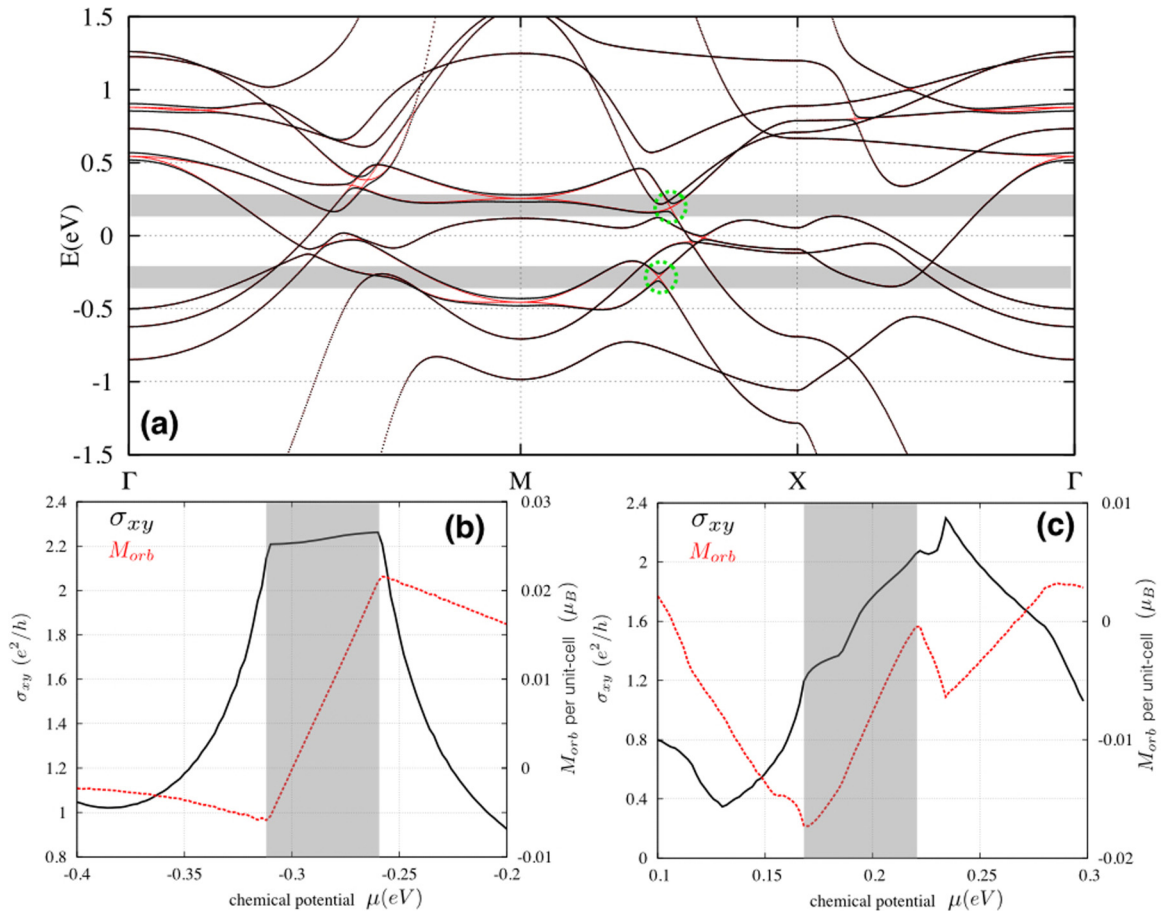


FIG. 7. (Color online) (a) Electronic band structures for minority spin near the Fermi level for a free-standing Fe bilayer with atomic SOI (black) and without atomic SOI (red), obtained from tight-binding calculations. The Dirac fermions are depicted by green dotted circles. (b) and (c) Hall conductivity and orbital magnetization as a function of the chemical potential μ . (b) μ ranges from -0.4 to -0.2 eV. (c) μ ranges from 0.1 to 0.3 eV.

an integration over μ , the orbital magnetization is calculated from the eight-band tight-binding model for a free-standing Fe monolayer (Fig. 5). Like the Hall conductivity, the result is decomposed into the two-band and the six-band contributions. The calculated magnetization exhibits a significant increase as a function of μ when μ is set inside the Dirac mass gap. The breakdown into the two contributions shows that the increase is mainly due to the six-band electronic states, indicating that the orbital moment near $\mu = 0$ mainly comes from an orbital motion of electrons along the chiral edge modes. In fact, $\partial M/\partial\mu$ is nearly quantized in the unit of e/hc , which counts the number of chiral edge modes inside the Dirac gap.

V. SUBSTRATE, ELECTRIC GATE VOLTAGE AND MULTIPLE-LAYER EFFECTS, AND THE hcp Co(111) MONOLAYER CASE

The Dirac fermions found in a free-standing Fe monolayer are robust against various perturbations, such as an oxide substrate, an out-of-plane applied electric field (e.g., electric gate voltage applied perpendicular to the layer), and multiple-layer effects. First, being a doubly degenerate point in an electronic energy band structure, the dual magnetic monopole (charge) discussed above is a stable point defect in the three-

dimensional parameter space subtended by k_x , k_y , and λ_{so} ; they cannot disappear by themselves. The symmetry property $H^*(\mathbf{k}, \lambda_{so}) = H(-\mathbf{k}, -\lambda_{so})$ further requires these defects to be in the $\lambda_{so} = 0$ plane, which guarantees the existence of massive Dirac fermions even for small λ_{so} . To annihilate these Dirac fermions, one generally needs to either reinvert the band inversion between the $3d_{xy}$ band and the $4s-3d_{x^2-y^2}$ hybrid band, or reduce completely the interlayer couplings among the $4s$ orbital, the $3d_{xy}$ orbital, and the $3d_{x^2-y^2}$ orbital. Unlike out-of-plane $3d$ orbitals, however, these in-plane $3d$ orbitals are influenced only slightly by the substrate and the out-of-plane electric field. As a result, we can readily find the massive Dirac fermions of the same origin even in the presence of various perturbations.

Figure 2 shows an electronic band structure for an Fe (001) monolayer with an MgO(001) substrate, where every Fe atom is located right above the oxygen of the MgO substrate. Due to crystal fields from these oxygens, three out-of-plane $3d$ orbital bands are brought up into a higher-energy region. Due to the charge neutrality, the Dirac fermions formed by the d_{xy} orbital and the $4s-3d_{x^2-y^2}$ hybrid orbitals become lower in energy than the Fermi level ($E \simeq -0.6$ eV). The size of the SOC-induced Dirac gap is estimated to be around 60 meV from the *ab initio* band calculation. The applied out-of-plane electric field has

little effect on these Dirac fermions either. Even under a very large out-of-plane electric field (± 1 V/Å), four Dirac fermions are barely affected [53].

Figure 7 shows an electronic band structure obtained from a tight-binding model for a free-standing Fe bilayer, where the number of massive Dirac fermions is doubled. Due to interlayer hoppings, a Dirac fermion from one layer and that from the other repel each other in energy. When the chemical potential is around these Dirac gaps, the transverse conductivity shows a peak structure with its maximum value around $2e^2/h$. The out-of-plane orbital magnetization increases as a function of the chemical potential inside the gaps. These features are essentially same as in the free-standing Fe monolayer case.

A comparison between an existing *ab initio* band calculation [16] and tight-binding analysis indicates that the massive Dirac fermions of the same kind are also induced by the atomic spin-orbit interaction in a minority-spin band in a hcp Co(111) monolayer with perpendicular magnetization. Thereby, d_{xz} and d_{yz} orbital bands comprise two massive Dirac fermions with positive mass at the K and K' point, respectively, which correspond to 4π magnetic charge at the M point in the Fe(001) monolayer case. Meanwhile, $4s$, $d_{x^2-y^2}$, and d_{xy} orbitals form six massive Dirac fermions with positive mass along the high symmetric k lines connecting Γ and $K(K')$ and two massive Dirac fermions with negative mass at K and K' , respectively. These result in a valence band with the Chern number $+2$, where the band has $4s$ character at Γ and d_{xy, x^2-y^2} characters at the Brillouin zone boundary. Due to the difference between the nominal valence of an iron atom and a cobalt atom, the

Dirac fermions in the Co(111) monolayer appear in a lower energy region than those in the Fe(001) monolayer case.

VI. CONCLUSION

Massive Dirac fermions are discovered near the Fermi level of an electronic band structure of Fe ultrathin film. The Dirac gap is induced by atomic spin-orbit coupling on the order of 50 meV. The topological gap opening results from a band inversion between a $3d_{xy}$ orbital band and a $4s-3d_{x^2-y^2}$ hybrid orbital band, giving rise to a finite Chern number in a valence band. Inside the gap, the Hall conductivity (versus chemical potential) exhibits a plateaulike structure with nearly quantized values, while orbital magnetization (versus chemical potential) increases rapidly due to the macroscopic orbital moment induced by topological chiral edge modes. The magnitude of the calculated orbital magnetization due to the chiral edge current is on the same order of the experimental literature value in [54], being hardly negligible in general. Massive Dirac fermions in Fe ultrathin film are shown to be robust against perpendicular inversion symmetry breaking (such as substrates or electric gate voltages) as well as the multilayer effect. More importantly, we found in Fe(001)/MgO(001) that the massive Dirac fermions are nicely separated from other dispersive bulk bands in energy, which may give a useful hint to explore a possible “Chern insulator” in transition-metal ferromagnetic thin film. Considering the richness of the transition metals with various substrates, we anticipate that Dirac fermion physics and Chern insulators may be observed experimentally in transition-metal thin films in the future.

-
- [1] K. S. Novoselov *et al.*, *Science* **306**, 666 (2004); *Nature (London)*, **438**, 197 (2005).
- [2] Y. Zhang *et al.*, *Nature (London)* **438**, 201 (2005).
- [3] C. W. J. Beenakker, *Rev. Mod. Phys.* **80**, 1337 (2008).
- [4] A. H. Castro Neto *et al.*, *Rev. Mod. Phys.* **81**, 109 (2009).
- [5] Z. Qiao, S. A. Yang, W. Feng, W.-K. Tse, J. Ding, Y. Yao, J. Wang, and Q. Niu, *Phys. Rev. B* **82**, 161414(R) (2010).
- [6] W.-K. Tse, Z. Qiao, Y. Yao, A. H. MacDonald, and Q. Niu, *Phys. Rev. B* **83**, 155447 (2011).
- [7] M. T. Johnson, P. J. H. Bloemen, F. J. A. den Broeder, and J. J. de Vries, *Rep. Prog. Phys.* **59**, 1409 (1996).
- [8] U. Gradmann and J. Muller, *Phys. Status Solidi* **27**, 313 (1968).
- [9] P. F. Carcia, A. D. Meinhardt, and A. Suna, *Appl. Phys. Lett.* **47**, 178 (1985).
- [10] P. F. Carcia, *J. Appl. Phys.* **63**, 5066 (1988).
- [11] W. P. Zeper *et al.*, *J. Appl. Phys.* **65**, 4971 (1989).
- [12] J. G. Gay and R. Richter, *Phys. Rev. Lett.* **56**, 2728 (1986); *J. Appl. Phys.* **61**, 3362 (1987).
- [13] P. Bruno, *Phys. Rev. B* **39**, 865(R) (1989).
- [14] C. Chappert and P. Bruno, *J. Appl. Phys.* **64**, 5736 (1988).
- [15] G. H. O. Daalderop, P. J. Kelly, and M. F. H. Schuurmans, *Phys. Rev. B* **41**, 11919 (1990).
- [16] G. H. O. Daalderop, P. J. Kelly, and M. F. H. Schuurmans, *Phys. Rev. B* **50**, 9989 (1994).
- [17] C.-G. Duan, J. P. Velev, R. F. Sabirianov, Z. Zhu, J. Chu, S. S. Jaswal, and E. Y. Tsymlal, *Phys. Rev. Lett.* **101**, 137201 (2008).
- [18] M. K. Niranjan, C.-G. Duan, S. S. Jaswal, and E. Y. Tsymlal, *Appl. Phys. Lett.* **96**, 222504 (2010).
- [19] L. Xu and S. Zhang, *J. Appl. Phys.* **111**, 07C501 (2012).
- [20] H. Ohno, D. Chiba, F. Matsukura, T. Omiya, E. Abe, T. Dietl, Y. Ohno, and K. Ohtani, *Nature (London)* **408**, 944 (2000).
- [21] D. Chiba, M. Yamanouchi, F. Matsukura, and H. Ohno, *Science* **301**, 943 (2003).
- [22] M. Weisheit *et al.*, *Science* **315**, 349 (2007).
- [23] T. Maruyama, Y. Shiota, T. Nozaki, K. Ohta, N. Toda, M. Mizuguchi, A. A. Tulapurkar, T. Shinjo, M. Shiraishi, S. Mizukami, Y. Ando, and Y. Suzuki, *Nat. Nanotech.* **4**, 158 (2009).
- [24] Y. Shiota *et al.*, *Appl. Phys. Express* **2**, 063001 (2009).
- [25] S.-S. Ha *et al.*, *Appl. Phys. Lett.* **96**, 142512 (2010).
- [26] T. Nozaki, Y. Shiota, M. Shiraishi, T. Shinjo, and Y. Suzuki, *Appl. Phys. Lett.* **96**, 022506 (2010).
- [27] W.-G. Wang, M. Li, S. Hageman, and C. L. Chien, *Nat. Mater.* **11**, 64 (2012).
- [28] K. Nakamura, R. Shimabukuro, Y. Fujiwara, T. Akiyama, T. Ito, and A. J. Freeman, *Phys. Rev. Lett.* **102**, 187201 (2009).
- [29] E. Wimmer, H. Krakauer, M. Weinert, and A. J. Freeman, *Phys. Rev. B* **24**, 864 (1981).
- [30] M. Weinert, E. Wimmer, and A. J. Freeman, *Phys. Rev. B* **26**, 4571 (1982).
- [31] K. Nakamura, T. Ito, A. J. Freeman, L. Zhong, and J. Fernandez-de-Castro, *Phys. Rev. B* **67**, 014420 (2003).

- [32] U. von Barth and L. Hedin, *J. Phys. C* **5**, 1629 (1972).
- [33] H. L. Meyerheim, R. Popescu, N. Jedrecy, M. Vedpathak, M. Sauvage-Simkin, R. Pinchaux, B. Heinrich, and J. Kirschner, *Phys. Rev. B* **65**, 144433 (2002).
- [34] W. A. Harrison, *Electronic Structure and The Properties of Solids* (Dover, New York, 1989).
- [35] G. E. Volovik, *Zh. Eksp. Teor. Fiz.* **94**, 123 (1988) [*Sov. Phys. JETP* **67**, 1804 (1988)].
- [36] V. M. Yakovenko, *Phys. Rev. Lett.* **65**, 251 (1990).
- [37] X. L. Qi, Y. S. Wu, and S. C. Zhang, *Phys. Rev. B* **74**, 085308 (2006).
- [38] D. J. Thouless, M. Kohmoto, M. P. Nightingale, and M. den Nijs, *Phys. Rev. Lett.* **49**, 405 (1982).
- [39] M. Kohmoto, *Ann. Phys. (N.Y.)* **160**, 343 (1985).
- [40] M. V. Berry, *Proc. R. Soc. London, Ser. A* **392**, 45 (1984).
- [41] B. Simon, *Phys. Rev. Lett.* **51**, 2167 (1983).
- [42] R. Prange and S. Girvin, *The Quantum Hall Effect* (Springer-Verlag, New York, 1987).
- [43] W. P. Su, J. R. Schrieffer, and A. J. Heeger, *Phys. Rev. Lett.* **42**, 1698 (1979).
- [44] B. I. Halperin, *Phys. Rev. B* **25**, 2185 (1982).
- [45] A. J. Niemi and G. W. Semenoff, *Phys. Rep.* **135**, 99 (1986).
- [46] Y. Hatsugai, *Phys. Rev. Lett.* **71**, 3697 (1993).
- [47] T. Thonhauser, D. Ceresoli, D. Vanderbilt, and R. Resta, *Phys. Rev. Lett.* **95**, 137205 (2005).
- [48] D. Ceresoli, T. Thonhauser, D. Vanderbilt, and R. Resta, *Phys. Rev. B* **74**, 024408 (2006).
- [49] D. Xiao, J. Shi, and Q. Niu, *Phys. Rev. Lett.* **95**, 137204 (2005).
- [50] J. Shi, G. Vignale, D. Xiao, and Q. Niu, *Phys. Rev. Lett.* **99**, 197202 (2007).
- [51] P. Streda, *J. Phys. C* **15**, L717 (1982).
- [52] R. Shindou and N. Nagaosa, *Phys. Rev. Lett.* **87**, 116801 (2001).
- [53] K. Nakamura, T. Akiyama, T. Ito, M. Weinert, and A. J. Freeman, *Phys. Rev. B* **81**, 220409(R) (2010).
- [54] J. Stohr and H. Siegmann, *Magnetism*, Solid-State Sciences (Springer, Berlin, 2006).